ARTICLES
https://doi.org/10.1038/s41563-019-0415-3
nature materials

Formation of two-dimensional transition metal oxide nanosheets with nanoparticles as intermediates

Juan Yang[1,2,3], Zhiyuan Zeng[1,8], Jun Kang[1,8], Sophia Betzler[1], Cory Czarnik[4], Xiaowei Zhang[1], Colin Ophus[5], Chang Yu[2], Karen Bustillo[5], Ming Pan[4], Jieshan Qiu[2,6*], Lin-Wang Wang[1*] and Haimei Zheng[1,7*]

Two-dimensional (2D) materials have attracted significant interest because of their large surface-to-volume ratios and electron confinement. Compared to common 2D materials such as graphene or metal hydroxides, with their intrinsic layered atomic structures, the formation mechanisms of 2D metal oxides with a rocksalt structure are not well understood. Here, we report the formation process for 2D cobalt oxide and cobalt nickel oxide nanosheets, after analysis by in situ liquid-phase transmission electron microscopy. Our observations reveal that three-dimensional (3D) nanoparticles are initially formed from the molecular precursor solution and then transform into 2D nanosheets. Ab initio calculations show that a small nanocrystal is dominated by positive edge energy, but when it grows to a certain size, the negative surface energy becomes dominant, driving the transformation of the 3D nanocrystal into a 2D structure. Uncovering these growth pathways, including the 3D-to-2D transition, provides opportunities for future material design and synthesis in solution.

Two-dimensional (2D) materials have shown superior performance in catalysis, sensing and many other surface-enhanced applications[1–6]. Over the past decade, significant advances have been made in the synthesis of a variety of 2D nanomaterials, including graphene, metal chalcogenides, metal oxides and metal hydroxides[7–12]. Recently, the formation of 2D zeolite nanosheets with nanoparticles as seeds has also been reported[13]. For naturally layered 2D nanostructures, such as graphene or metal hydroxides, ab initio calculations show that 2D morphologies can be achieved as a result of the growth rate of the high-energy facets in the lateral direction being higher than that of the low-energy facets in the vertical direction[14–17]. This has been recognized as the most favourable growth mechanism for obtaining layered 2D nanostructures in wet-chemical syntheses. However, how and why non-layered crystals (for example, rocksalt transition metal oxides and metal chalcogenides) form 2D nanosheets is not obvious[18–24]. It has been speculated that the organic ligand molecules may act as a 'template' for 2D growth by selectively tuning the energy of specific facets or by triggering the oriented attachment of primary blocks[22,24–26]. Nevertheless, the growth mechanisms of non-layered 2D nanosheets initiated from a molecular precursor solution are largely unknown. An understanding of the 2D nanostructure growth mechanisms is of vital importance to the controlled synthesis of 2D nanocrystals in solution.

Liquid-phase transmission electron microscopy (TEM) provides an opportunity to elucidate the solution growth mechanisms of nanocrystals by direct observation of the dynamic growth processes[27–29]. Here, we study the formation of transition metal oxide (cobalt oxide, cobalt nickel oxide and nickel oxide) nanosheets in a liquid cell under TEM. This advanced imaging, with high signal-to-noise ratio and high spatial and temporal resolution, allows us to uncover the atomic pathways of 2D nanostructure formation, which involve 3D nanoparticle intermediates and a 3D-to-2D transformation. Our experiments also show that nickel oxide prefers to retain its 3D nanoparticle geometry under the growth conditions used. Density functional theory (DFT) calculations were used to elucidate the driving force for the 3D-to-2D transformations.

The precursor growth solution was prepared by dissolving $Co(acetylacetonate)_2$ ($Co(acac)_2$) and/or $Ni(acac)_2$ in a solvent mixture of oleylamine, oleic acid and benzyl ether (4.5:4.5:1 volume ratio). For the growth of cobalt nickel oxide, a $Ni(acac)_2$ to $Co(acac)_2$ molar ratio of 1:1 was used as the precursor solution. Approximately 100 nl of the solution was loaded into a liquid cell, yielding a thin liquid layer (~100 nm, defined by the spacer thickness) sandwiched between two silicon nitride (SiN_x) membranes. During imaging, the liquid thickness may vary due to bubble formation during electron beam illumination (10–20 nm thickness, see Methods). We used a ThermoFisher (previously FEI F20 Tecnai) transmission electron microscope equipped with an advanced high-speed detector (K2 IS camera, Gatan). An electron current density of 2,000–8,000 e^- Å^{-2} s^{-1} was maintained during imaging. We also used a JEOL 2100 microscope with a charge-coupled device (CCD) camera to capture the growth process with a large field of view, with the electron beam current density kept at 10–50 e^- Å^{-2} s^{-1}; the liquid thickness was ~60 nm. In spite of variations in liquid thickness and different electron dose rates, the growth characteristics for each system (cobalt oxide, cobalt nickel oxide or nickel oxide) were

[1]Materials Sciences Division, Lawrence Berkeley National Laboratory, Berkeley, CA, USA. [2]State Key Lab of Fine Chemicals, School of Chemical Engineering, Liaoning Key Lab for Energy Materials and Chemical Engineering, Dalian University of Technology, Dalian, China. [3]School of Chemical Engineering and Technology, Xi'an Jiaotong University, Xi'an, China. [4]Gatan Inc., Pleasanton, CA, USA. [5]National Center for Electron Microscopy, Molecular Foundry, Lawrence Berkeley National Laboratory, Berkeley, CA, USA. [6]State Key Laboratory of Chemical Resource Engineering, College of Chemical Engineering, Beijing University of Chemical Technology, Beijing, China. [7]Department of Material Science and Engineering, University of California, Berkeley, CA, USA. [8]These authors contributed equally: Zhiyuan Zeng, Jun Kang. *e-mail: jqiu@dlut.edu.cn; lwwang@lbl.gov; hmzheng@lbl.gov

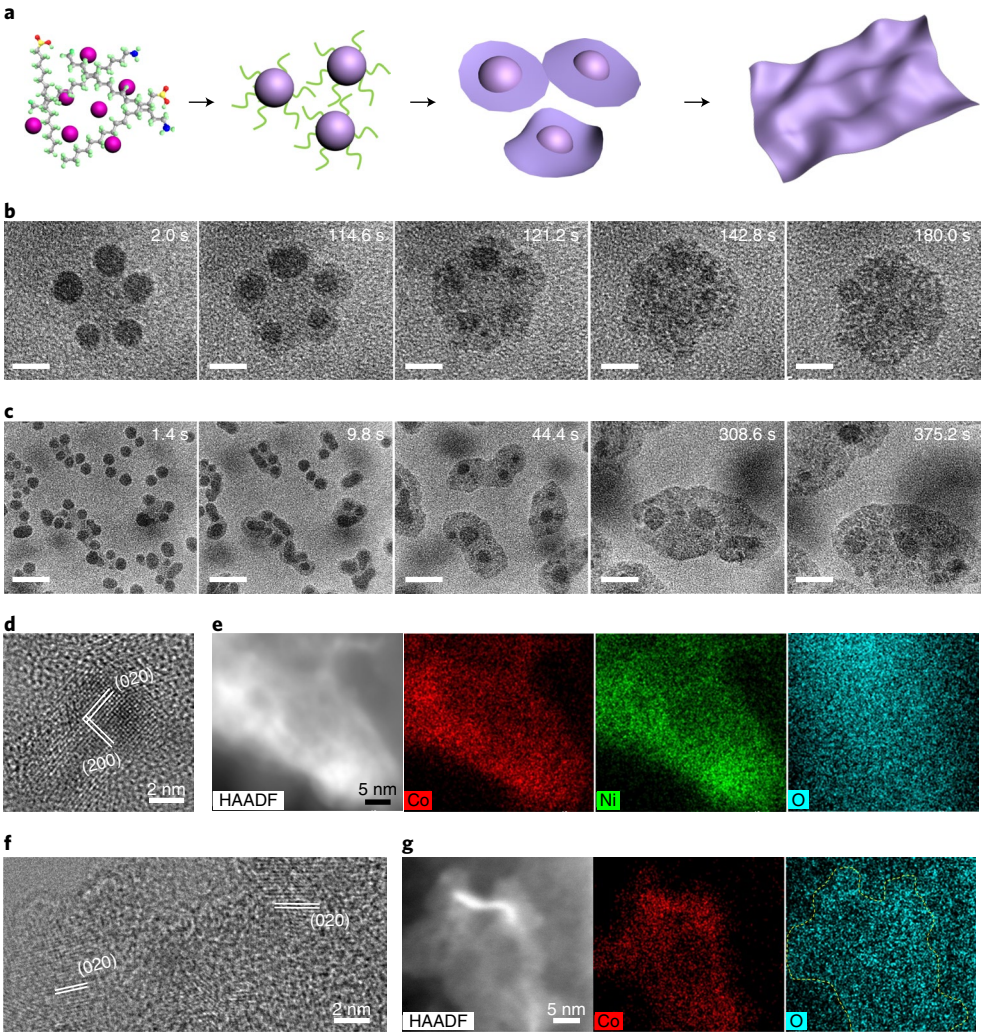

Fig. 1 | Growth and transformations of cobalt oxide and cobalt nickel oxide nanocrystals into 2D nanosheets. a, Schematic showing the formation of a 2D nanosheet from a molecular precursor solution with the pathway of 3D nanoparticle growth and subsequent 3D-to-2D transformations. **b**, Sequential images show a few cobalt nickel oxide nanoparticles transforming into a 2D nanosheet. The same growth pathway is found in the cobalt oxide system (Supplementary Fig. 1a). Scale bars, 5 nm. **c**, Sequential images showing the formation of cobalt nickel oxide nanosheets through the growth of 3D nanoparticles and 3D-to-2D transformations. Scale bars, 10 nm. **d**, High-resolution image of cobalt nickel oxide nanoparticles at the transformation into a 2D nanosheet. **e**, High-angle annular dark field (HAADF) image of a cobalt nickel oxide nanosheet and EDS maps showing the Co, Ni and O elemental distribution. **f**, High-resolution image of cobalt oxide nanoparticles at the transformation into a 2D nanosheet. **g**, HAADF image of a cobalt oxide nanosheet and EDS maps showing the Co and O elemental distribution.

self-consistent, suggesting that the observed 3D-to-2D transformations are arising from the intrinsic material properties.

Many nanoparticles are formed under the electron beam illumination in the early stage of growth[27]. As shown in Fig. 1a–c (see also Supplementary Videos 1–3 and Supplementary Fig. 1a), each nanocrystal is single-crystalline and rotates frequently during growth. In the first step of the 3D nanoparticles transforming into 2D nanostructures, the nanoparticles spread out. The spreading edges appear to be much thinner than the nanoparticle core, highlighting the distinct 3D-to-2D (nanoparticle to nanosheet) transformation. It is noted that such 2D growth with 3D nanoparticles as intermediates is different from 2D growth with surfactant molecules as a 'soft template'[22,24,26], where the system continuously grows in 2D with a given thickness. Here, the average particle size at the 3D-to-2D transition is 3.8 ± 0.3 nm for cobalt oxide (Supplementary Fig. 1b,c) and 4.3 ± 0.7 nm for cobalt nickel oxide (Supplementary Fig. 2). The thickness of the nanosheets is estimated to be in the range of ~0.6–1.1 nm (see Methods). From the high-resolution TEM images in Fig. 1d,f, the cobalt oxide and cobalt nickel oxide nanosheets are seen to have a rocksalt crystal structure. Energy-dispersive X-ray spectroscopy (EDS) elemental maps show the presence of cobalt, nickel and oxygen in the nanosheets (Fig. 1e,g). For the cobalt nickel oxide nanosheets, the atomic ratio of Ni to Co is close to 1:1 (Supplementary Fig. 3), which is consistent with the precursor solution.

We tracked the growth trajectories of individual nanosheets with high-resolution imaging using the K2 IS detector (Fig. 2 and Supplementary Video 4). Typically, a nanoparticle with a cubic shape is formed at the early stage. When it resides along the [002] viewing axis, the {200} and {220} facets are identifiable (see the 3D model and 2D projection in Fig. 2a). The faster growth of the four {220} facets temporarily results in a 'butterfly' shape; however, the subsequent growth of all facets leads to a square in the 2D projection (Fig. 2b). Anisotropic growth is also evidenced by other cobalt oxide nanosheets (Supplementary Video 5 and Supplementary Fig. 6), which is probably due to the higher energy of the {220} facets[25,30–32]. The projected particle size evolution with time (Fig. 2c)

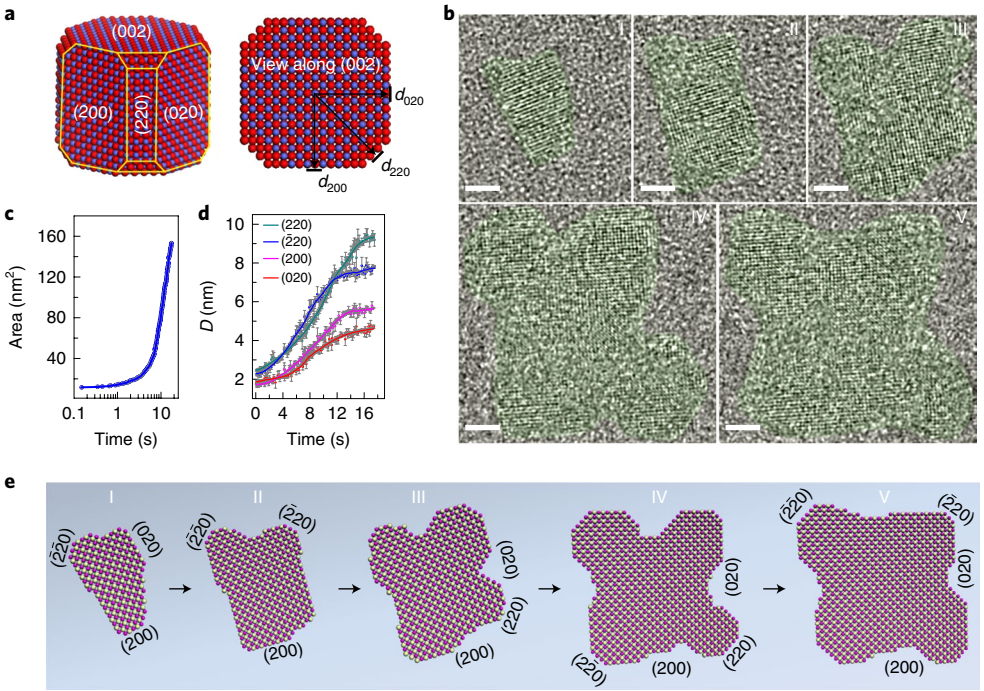

Fig. 2 | Tracking of cobalt oxide nanosheet development with high resolution. a, Atomic model of a cobalt oxide structure and its projection along the [002] view zone axis. The distances from the crystal centre to each of the (200), (220) and (020) facets are marked. **b**, Sequential images from Supplementary Video 4 show the formation of a cobalt oxide nanosheet. Colour is used to guide the eyes (original images are provided in Supplementary Fig. 5). I, 5.23 s; II, 6.18 s; III, 9.18 s; IV, 14.0 s; V, 14.7 s. Scale bars, 2 nm. **c**, Projected particle size as a function of time during the growth of cobalt oxide nanocrystals undergoing the 3D-to-2D transformations. **d**, The average centre-to-facet distance as a function of time. Error bars, standard deviation. **e**, Highlighted growth pathway of nanosheet formation based on the TEM images in **b**.

shows slower growth at the early stage (0–4 s; 3D nanoparticle growth) than at the later stage (4–14 s; 2D nanosheet growth). The transition from a 3D nanoparticle to a 2D nanosheet takes place at ~4 s, corresponding to a particle size of 4.0 nm (Fig. 2d). It is noted that it is hard to distinguish the 3D-to-2D transition from the high-resolution images alone due to the phase contrast. Our conclusions are supported by measurements of a large number of nanoparticles from both high-resolution and low-magnification videos.

We also studied the effects of neighbouring nanoparticles on the morphological development of a 2D nanosheet. Figure 3a (Supplementary Video 6) shows the devlopment of a cobalt oxide nanoparticle into a nanosheet (highlighted in green) in the presence of a nanoparticle (highlighted in brown) in the near distance. The projected particle size as a function of time (Fig. 3b) shows a similar trend as that in Fig. 2c, highlighting the two stages—3D and 2D—of growth. The 2D growth after the 3D-to-2D transition may be driven by the directional growth kinetics. However, due to the hindering effects from the adjacent nanoparticle, the growth of the (020) facet appears to be slower than that of the (200) facet (Fig. 3c). This observation suggests that the configurations of neighbouring nanoparticles influence the evolution of nanosheet morphology.

Figure 3d shows the interactions between two nanosheets, both of which reside along the [002] viewing axis. Atomic rearrangement during growth can be observed (Supplementary Video 7). During the period from 0 to 50 s (the initial time is arbitrary), each nanosheet develops continuously while there is a gap between them (see magnified images). In the following period from 50 to 85 s, the two nanosheets make contact at one, then many points, and eventually completely attach to one another. During attachment, crystal orientation rearrangement is observed and the appearance of {220} facets expedites the attachment process. It is energetically favourable for the high-surface-energy facets to attach together[25,33]. The surface ligands adsorbed on the metal oxide surface may also play an important role in nanosheet attachment. The formation of a large nanosheet by the attachment of smaller nanosheets can be understood by the conventional growth model of eliminating surfaces and interfaces to reduce the system energy.

Demonstration of 2D growth involving 3D-to-2D transformations represents a significant advance in the study of 2D material growth mechanisms. Such a growth pathway is different from 2D nanosheet formation through oriented attachment of the primary 3D nanocrystals[25,34] and the 'soft template'-assisted growth of 2D nanostructures[26,35,36]. Our in situ experiments demonstrate that the 3D-to-2D transformations arise spontaneously from the intrinsic material properties, and are independent of the liquid confinement or electron beam effects (for discussions of liquid thickness, electron beam effects and image processing, see Methods). To confirm this, we synthesized cobalt oxides outside of the liquid cell TEM, and 2D cobalt oxide nanosheets could be obtained, as shown in Supplementary Fig. 13.

In addition, we carried out the growth of nickel oxide nanocrystals under the same experimental conditions. From Supplementary Video 8, it is clear that some nanoparticles attempt to spread out during growth, but they fail to develop into nanosheets (Fig. 4 and Supplementary Figs. 15a and 16). All nickel oxide nanoparticles maintain 3D nanoparticles during the entire growth process. The energy barrier for nickel oxide nanocrystals to transform into a 2D nanosheet appears to be much higher, as will be discussed in detail in nickel oxide calculations (see Methods).

DFT calculations were performed to reveal the reason why the cobalt oxide (or cobalt nickel oxide) nanoparticles transform into 2D nanosheets after reaching a certain size. The 3D-to-2D transition

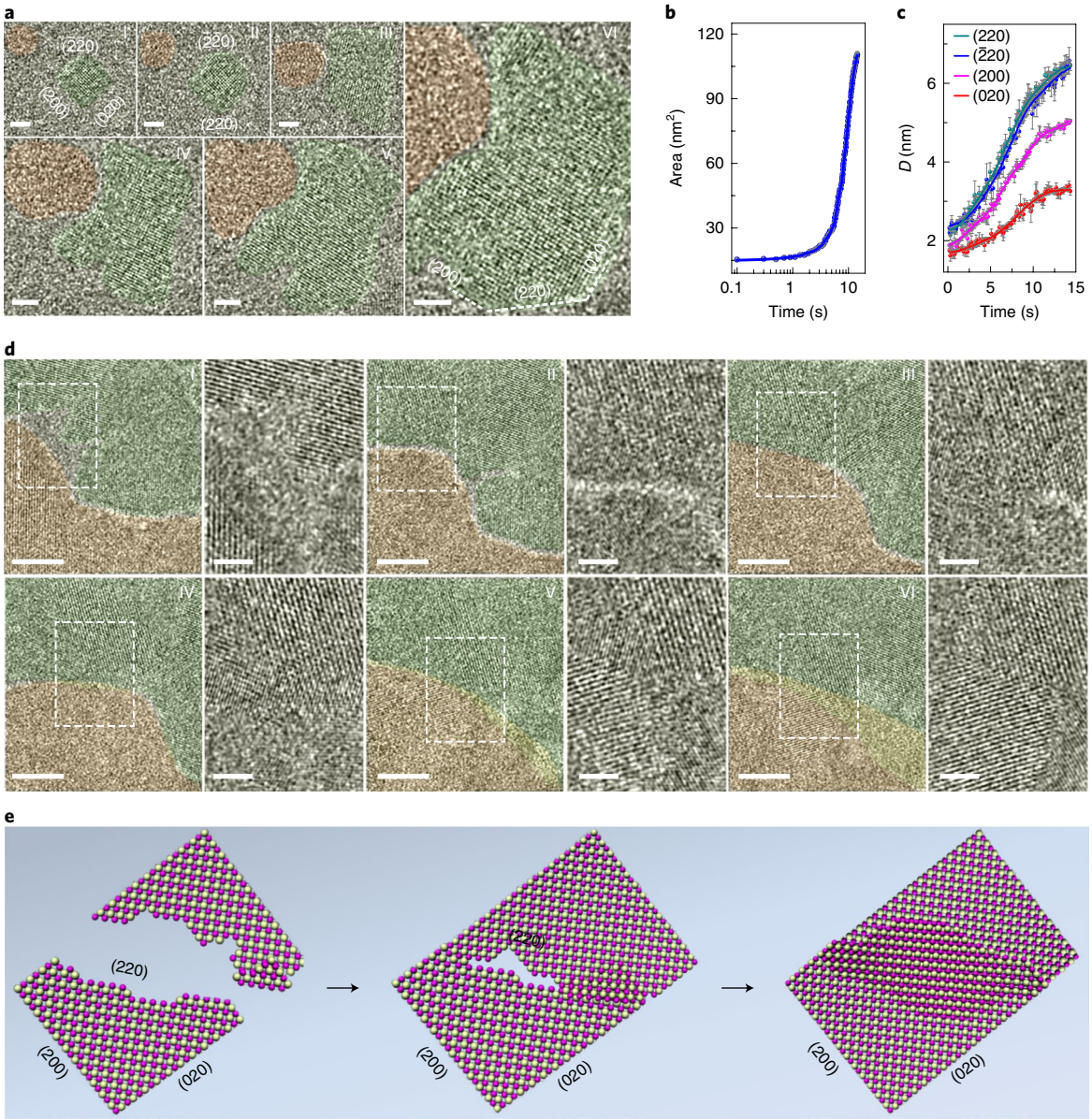

Fig. 3 | The interaction and attachments between two cobalt oxide nanosheets. a, Sequential images showing the growth of a cobalt oxide nanosheet in the presence of another nanoparticle in the adjacent distance (colours are used to guide the eye; for the original images see Supplementary Fig. 7). I, 0.98 s; II, 2.86 s; III, 7.88 s; IV, 10.64 s; V, 13.75 s; VI, 16.70 s. Scale bars, 2 nm. **b**, Projected area of the cobalt oxide nanocrystal as a function of time during growth. **c**, Measured average distance from the crystal centre to each facet as a function of time. Error bars, s.d. **d**, Sequential images showing the attachment of two nanosheets (for the original images see Supplementary Fig. 8). I, 21.06 s; II, 42.46 s; III, 63.49 s; IV, 73.83 s; V, 91.07 s; VI, 96.53 s. Magnified TEM images from the areas within white dashed rectangles are presented on the right of each image. Scale bars, 5 nm in original TEM images (left) and 2 nm in the magnified TEM images (right). **e**, Schematic highlighting the interaction and attachment of two nanosheets.

is accompanied by a sudden change in shape, as shown above (the thickness/height of the system reduces); this is much like a first-order phase transition. It would be difficult to explain this transition by directional growth kinetics. Thus, the thermodynamic driving force is proposed to be dominant for such a 3D-to-2D transition. Furthermore, Fourier transform infrared (FT-IR) spectroscopy and EDS elemental analysis reveal that the actual ligands on the surface of cobalt oxides are mainly oleylamine molecules (Supplementary Figs. 18 and 19). To further confirm this, we carried out synthesis experiments using solely oleic acid as ligand. However, no reaction product could be purified and characterized. These results are consistent with previous reports that metal oxides can be preferentially coordinated by alkylamine ligands, and the incorporation of oleic acid ligands can assist by improving the nanocrystal dispersion and stability[27,35,37]. Considering that oleylamine ligands bind to the nanoparticle surfaces during growth, we estimated the ligand–surface binding energies for the different facets. Because the oleylamine ligands interact with cobalt oxide only through the -NH_2 group, we simplified the calculation by using methylamine instead of oleylamine. By using methylamine, the alkyl chain–chain van der Waals interaction can be neglected. As shown in a previous work[36], the chain–chain interaction in the solvent and at the surface may cancel each other, so replacing oleylamine by methylamine will not significantly affect the calculated binding energy. The ligand adsorption on the (100) and (110) surfaces is shown in Fig. 5a and Supplementary Fig. 20. The bare (100) and (110) surfaces are found

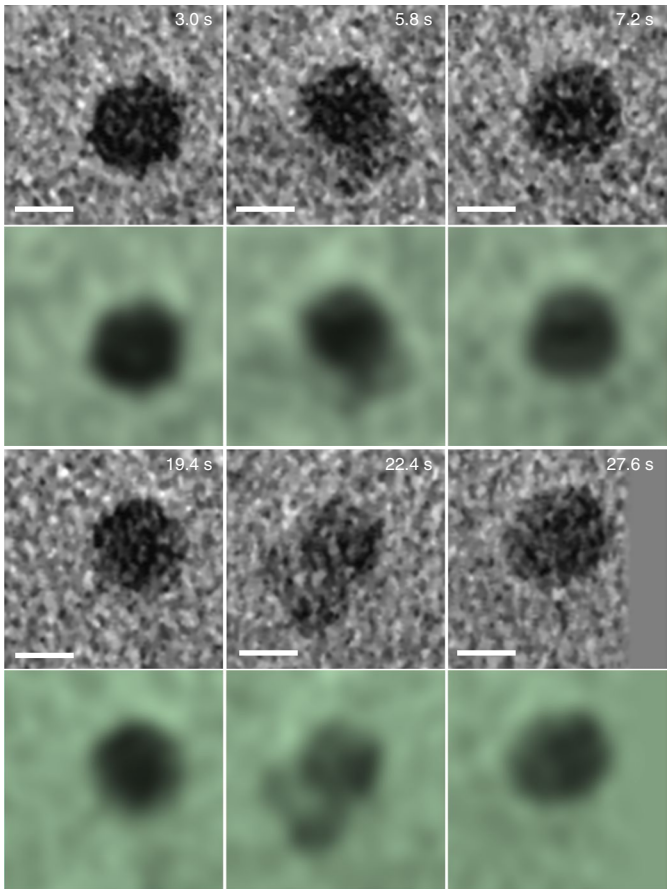

Fig. 4 | Sequential images show the growth of nickel oxide nanocrystals. The 3D nanoparticle does not transform into a 2D structure, although there are attempts to spread out (5.8 s, 22.4 s). Each colour image, corresponding to the original image above, highlights the image contrast variations at the edges of the nanoparticle to show the attempts to spread out. Scale bars, 2 nm.

to have positive surface energy. However, with amine passivation, the surface energies for (100) and (110) are calculated to be −7.28 and 27 meV Å^{-2} (Supplementary Table 1), respectively. In addition, when the amine binding effect in the solvent is considered (for details of calculations see Methods), the surface energies for (100) and (110) become −1.7 and 31 meV Å^{-2} (Supplementary Table 2). All the calculations show that the {100} facets are more favourable than the {110} facets during growth, which is consistent with the observation that the nanocrystals are mainly {100}-terminated. More importantly, the negative {100} surface energy drives the system to have a larger area of {100} facet, so a 2D nanosheet instead of a 3D nanoparticle is preferred.

However, the favourable negative surface energy alone cannot explain the observed 3D-to-2D transitions. What is missing is the shape factor of the nanoparticles. Here, we use a simple model to describe the growth process by including the edge energy (corresponding to the nanoparticle shape). A similar model was also proposed recently[38] in which the surface energy is positive. In our model, the surface energy is calculated to be negative, and the competition between the negative surface energy and positive edge energy is highlighted here. Starting from a cubic nanoparticle with edge length L_0, such a 3D nanoparticle transforms into a 2D nanosheet by the sheet gradually growing underneath the nanoparticle (Fig. 5b). This simplified model is consistent with what we have observed in experiments; that is, a cubic nanoparticle spreads and transforms into a 2D nanosheet. Assuming that both the nanoparticle and the nanosheet consist of only {100} facets and the edges between neighbouring surfaces, the total energy of such a system can be expressed as

$$E = uE_s + vE_e + wE_b \ldots \quad (1)$$

Here, $E_s = -7.28$ meV Å^{-2}, $E_e = 158$ meV Å^{-1} and $E_b = -609$ meV Å^{-3} are the calculated surface energy, edge energy and bulk energy (for calculation details see Methods), while u, v and w are the surface area, edge length and volume of the whole system. It is noted that this expression is not affected by the discrete nature of the system at the smallest dimensions. One can effectively replace u, v and w by using the number of atoms on the surface, edge and bulk. The energy difference between a 2D nanosheet and the 3D nanoparticle ($\Delta E = E_{2D} - E_{3D}$) is calculated using equation (1). The results show that there is a critical size (L_C) for the 3D nanoparticle to transform into a 2D nanosheet, and L_C is dependent on the nanosheet thickness, T (Supplementary Fig. 21). For $T = 1$ nm, when the size (L_0) of the cobalt oxide nanoparticles is less than 3.0 nm, the 2D nanosheet has higher energy than a 3D nanoparticle and the 3D nanoparticle is preferred. When L_0 is larger than 3.0 nm, the nanosheet becomes more stable. The critical size of L_C is therefore ~3.0 nm. Such a crossover results from the competition between the negative surface energy and positive edge energy. For a large nanoparticle, the negative surface energy wins, while for a small nanoparticle, the positive edge energy dominates. The total energy evolution for the 3D-to-2D transformations can be calculated. The plots in Fig. 5c show the energy evolution of various nanoparticles of different initial sizes. When L_0 is within the range 3.0–4.4 nm, there is a kinetic energy barrier for the 3D-to-2D transformations. When L_0 is larger than 4.4 nm, the barrier disappears and the 3D-to-2D transition occurs spontaneously. It is also noted that defects can be important in the growth process. For example, Frenkel defects can form easily on the surface becauses there is more free space on the surface than in the bulk. The binding energy of the ligand–defect can be larger than that of the ligand–surface interaction, so the surface energy may be reduced further by the ligand–defect binding. This might facilitate the 3D-to-2D transformations.

The above ab initio calculation shows that 3D-to-2D transformations are governed by the competition between the negative surface energy and the positive edge energy. It is critical to have the negative surface energy as the driving force for the observed 3D-to-2D transformations. However, the negative surface energy is not a requirement for 2D growth as kinetic factors may play the dominant role. In this work, the system has a smaller overall barrier when a small nanoparticle first grows in 3D and it must kinetically overcome a barrier to transform into a 2D sheet. When the nanoparticle is sufficiently large, the barrier for the 3D-to-2D transformations is at a minimum. The calculated critical size (L_C) for the 3D-to-2D transition is 4.4 nm, without considering the ligand binding effects. However, when the amine binding effects are taken into account, a larger L_C value is obtained ($L_C \approx 8.0$ nm; Supplementary Figs. 22 and 23). This is much larger than the experimentally observed value (~3.8 nm) and the discrepancy may be caused by the fact that the nanoparticle geometry in the experiments is less ideal than the modelled one. However, the less ideal particle shape does not change the trend of the 3D-to-2D transformation. Calculations on the nickel oxide system show a similar trend but the critical size (L_C) for the 3D-to-2D transformation is much larger (see Methods and Supplementary Fig. 24). The {100} surface energy for nickel oxide is positive (~6 meV Å^{-2}), even with the amine binding effect. This indicates that the 3D-to-2D transformation is less likely to occur for small nanoparticles, which agrees with the experimental results.

Although the growth is often a kinetic process, the shape of a nanoparticle with given volume V is determined thermodynamically by free energy minimization. In most classical nucleation theories,

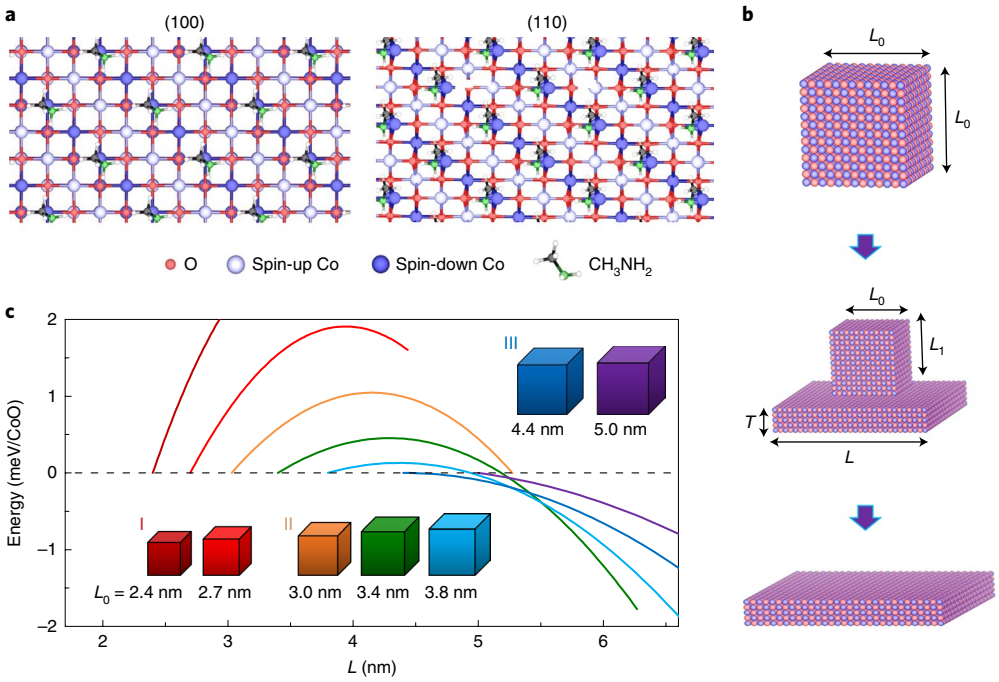

Fig. 5 | Energy evolution of cobalt oxide during the 3D-to-2D transition. a, The amine ligands adsorbed on cobalt oxide (100) and (110) surfaces. Red, O atoms; white and blue balls, Co atoms with spin-up and spin-down polarization, respectively. **b**, Simplified model showing the transformation from a 3D nanoparticle to a 2D nanosheet. The 3D-to-2D transformation proceeds by the 3D nanoparticle spreading out at the bottom of the nanoparticle. **c**, Total energy evolution of the cobalt oxide system as a function of spreading particle size *L* for nanoparticles with different initial sizes (L_0). Group I shows that, when L_0 is smaller than 3.0 nm, the 3D nanoparticle is more stable. Group II shows that, when L_0 is within the range of 3.0–4.4 nm, the 2D nanosheet is more stable, but there is a barrier for the 3D-to-2D transformations. Group III shows that, when L_0 is larger than 4.4 nm, there is no barrier for cobalt oxide to transform into a 2D nanosheet.

only a uniform surface (for example, a model spherical surface) is considered for surface energy estimation. Our work shows that it is necessary to consider the shape of a nanoparticle, for instance, to distinguish the surface and edge energies. Identifying the pathways for 2D nanosheets formation involving 3D-to-2D transformations provides critical insights into the design and synthesis of 2D materials.

Online content

Any methods, additional references, Nature Research reporting summaries, source data, statements of code and data availability and associated accession codes are available at https://doi.org/10.1038/s41563-019-0415-3.

Received: 26 October 2018; Accepted: 23 May 2019;
Published online: 8 July 2019

References

1. Deng, D. et al. Catalysis with two-dimensional materials and their heterostructures. *Nat. Nanotechnol.* **11**, 218–230 (2016).
2. Koppens, F. H. L. et al. Photodetectors based on graphene, other two-dimensional materials and hybrid systems. *Nat. Nanotechnol.* **9**, 780–793 (2014).
3. Lukatskaya, M. R. et al. Cation intercalation and high volumetric capacitance of two-dimensional titanium carbide. *Science* **341**, 1502–1505 (2013).
4. Nair, R. R. et al. Fine structure constant defines visual transparency of graphene. *Science* **320**, 1308 (2008).
5. Lv, R. et al. Transition metal dichalcogenides and beyond: synthesis, properties and applications of single- and few-layer nanosheets. *Acc. Chem. Res.* **48**, 56–64 (2015).
6. Gao, L. et al. Face-to-face transfer of wafer-scale graphene films. *Nature* **505**, 190–194 (2014).
7. Coleman, J. N. et al. Two-dimensional nanosheets produced by liquid exfoliation of layered materials. *Science* **331**, 568–571 (2011).
8. Geim, A. K. & Novoselov, K. S. The rise of graphene. *Nat. Mater.* **6**, 183–191 (2007).
9. Ma, R., Liang, J., Liu, X. & Sasaki, T. General insights into structural evolution of layered double hydroxide: underlying aspects in topochemical transformation from brucite to layered double hydroxide. *J. Am. Chem. Soc.* **134**, 19915–19921 (2012).
10. Sun, Y., Gao, S., Lei, F., Xiao, C. & Xie, Y. Ultrathin two-dimensional inorganic materials: new opportunities for solid state nanochemistry. *Acc. Chem. Res.* **48**, 3–12 (2015).
11. Wang, Q. & O'Hare, D. Recent advances in the synthesis and application of layered double hydroxide (LDH) nanosheets. *Chem. Rev.* **112**, 4124–4155 (2012).
12. Ma, R. & Sasaki, T. Two-dimensional oxide and hydroxide nanosheets: controllable high-quality exfoliation, molecular assembly and exploration of functionality. *Acc. Chem. Res.* **48**, 136–143 (2015).
13. Jeon, M. Y. et al. Ultra-selective high-flux membranes from directly synthesized zeolite nanosheets. *Nature* **543**, 690–694 (2017).
14. Gamble, F. R. et al. Intercalation complexes of Lewis bases and layered sulfides: a large class of new superconductors. *Science* **174**, 493–497 (1971).
15. Ha, B., Char, K. & Jeon, H. S. Intercalation mechanism and interlayer structure of hexadecylamines in the confined space of layered α-zirconium phosphates. *J. Phys. Chem. B* **109**, 24434–24440 (2005).
16. Jang, J. et al. Ultrathin zirconium disulfide nanodiscs. *J. Am. Chem. Soc.* **133**, 7636–7639 (2011).
17. Manna, L., Wang, Cingolani, R. & Alivisatos, A. P. First-principles modeling of unpassivated and surfactant-passivated bulk facets of wurtzite CdSe: a model system for studying the anisotropic growth of CdSe nanocrystals. *J. Phys. Chem. B* **109**, 6183–6192 (2005).
18. Gao, S. et al. Partially oxidized atomic cobalt layers for carbon dioxide electroreduction to liquid fuel. *Nature* **529**, 68–71 (2016).
19. Huang, X. et al. Freestanding palladium nanosheets with plasmonic and catalytic properties. *Nat. Nanotechnol.* **6**, 28–32 (2011).
20. Niu, J. et al. Novel polymer-free iridescent lamellar hydrogel for two-dimensional confined growth of ultrathin gold membranes. *Nat. Commun.* **5**, 3313 (2014).
21. Saleem, F. et al. Ultrathin Pt–Cu nanosheets and nanocones. *J. Am. Chem. Soc.* **135**, 18304–18307 (2013).

22. Sun, Z. et al. Generalized self-assembly of scalable two-dimensional transition metal oxide nanosheets. *Nat. Commun.* **5**, 3813 (2014).
23. Jia, Y. et al. Unique excavated rhombic dodecahedral $PtCu_3$ alloy nanocrystals constructed with ultrathin nanosheets of high-energy {110} facets. *J. Am. Chem. Soc.* **136**, 3748–3751 (2014).
24. Li, Z. & Peng, X. Size/shape-controlled synthesis of colloidal CdSe quantum disks: ligand and temperature effects. *J. Am. Chem. Soc.* **133**, 6578–6586 (2011).
25. Schliehe, C. et al. Ultrathin PbS sheets by two-dimensional oriented attachment. *Science* **329**, 550–553 (2010).
26. Son, J. S. et al. Large-scale soft colloidal template synthesis of 1.4-nm-thick CdSe nanosheets. *Angew. Chem. Int. Ed.* **48**, 6861–6864 (2009).
27. Liao, H. G. et al. Facet development during platinum nanocube growth. *Science* **345**, 916–919 (2014).
28. Yuk, J. M. et al. High-resolution EM of colloidal nanocrystal growth using graphene liquid cells. *Science* **336**, 61–64 (2012).
29. Li, D. et al. Direction-specific interactions control crystal growth by oriented attachment. *Science* **336**, 1014–1018 (2012).
30. Hansen, P. L. et al. Atom-resolved imaging of dynamic shape changes in supported copper nanocrystals. *Science* **295**, 2053–2055 (2002).
31. Tian, N., Zhou, Z. Y., Sun, S.-G., Ding, Y. & Wang, Z. L. Synthesis of tetrahexahedral platinum nanocrystals with high-index facets and high electro-oxidation activity. *Science* **316**, 732–735 (2007).
32. Urban, J. J., Talapin, D. V., Shevchenko, E. V. & Murray, C. B. Self-assembly of PbTe quantum dots into nanocrystal superlattices and glassy films. *J. Am. Chem. Soc.* **128**, 3248–3255 (2006).
33. Penn, R. L. & Banfield, J. F. Imperfect oriented attachment: dislocation generation in defect-free nanocrystals. *Science* **281**, 969–971 (1998).
34. Gao, S. et al. Ultrahigh energy density realized by a single-layer beta-$Co(OH)_2$ all-solid-state asymmetric supercapacitor. *Angew. Chem. Int. Ed.* **53**, 12789–12793 (2014).
35. Sun, S. et al. Monodisperse MFe_2O_4 (M = Fe, Co, Mn) nanoparticles. *J. Am. Chem. Soc.* **126**, 273–279 (2004).
36. Son, J. S. et al. Colloidal synthesis of ultrathin two-dimensional semiconductor nanocrystals. *Adv. Mater.* **23**, 3214–3219 (2011).
37. Puntes, V. F., Zanchet, D., Erdonmez, C. K. & Alivisatos, A. P. Synthesis of hcp-Co nanodisks. *J. Am. Chem. Soc.* **124**, 12874–12880 (2002).
38. Riedinger, A. et al. An intrinsic growth instability in isotropic materials leads to quasi-two-dimensional nanoplatelets. *Nat. Mater.* **16**, 743–748 (2017).

Acknowledgements

This work was funded by the US Department of Energy, Office of Science, Office of Basic Energy Sciences, Materials Sciences and Engineering Division under contract no. DE-AC02-05-CH11231 within the in situ TEM programme (KC22ZH). Work at the Molecular Foundry was supported by the Office of Science, Office of Basic Energy Sciences, of the US Department of Energy under contract no. DE-AC02-05CH11231. J.Y. and J.Q. acknowledge funding support from the Natural Science Foundation of China (nos 51802251 and U1508201). J.Y. also acknowledges funding support from the China Scholarship Council (201506060073) and China Postdoctoral Science Foundation (2018M631168). This work used resources of the National Energy Research Scientific Computing Center and the Oak Ridge Leadership Computing Facility through the INCITE project. The authors thank D. Zherebetskyy (L.-W.W.'s group) for useful discussions.

Author contributions

J.Y. designed and performed the experiments and analysed the experimental data. J.K. and L.-W.W. performed the DFT calculations. Z.Z., X.Z. and C.Y. provided reagents and analysed data. S.B. carried out the measurements and calibration of liquid thickness in the liquid cells. C.C. and M.P. provided part of the TEM characterization. C.O. and K.B. helped with image processing and materials structure analyses. J.Y. and H.Z. wrote the manuscript. All authors contributed to the overall scientific interpretation and editing of the manuscript. J.Q. supervised part of the experimental work. L.-W.W. supervised the theory part of this work. All work was carried out under the supervision of H.Z.

Competing interests

The authors declare no competing interests.

Additional information

Supplementary information is available for this paper at https://doi.org/10.1038/s41563-019-0415-3.

Reprints and permissions information is available at www.nature.com/reprints.

Correspondence and requests for materials should be addressed to J.Q., L.-W.W. or H.Z.

Publisher's note: Springer Nature remains neutral with regard to jurisdictional claims in published maps and institutional affiliations.

Methods

Chemicals. All chemicals were used as purchased from Sigma-Aldrich, including $Co(acetylacetonate)_2$ (99%), $Ni(acetylacetonate)_2$ (99%), oleylamine (98%), oleic acid (70%) and benzyl ether (99%). The growth solution was prepared by dissolving 0.1 mmol of $Co(acetylacetonate)_2$ in a surfactant/solvent mixture of oleylamine, oleic acid and benzyl ether (4.5:4.5:1 volume ratio in a total 1 ml solution). The binary metal salt precursor solutions with $Co(acetylacetonate)_2$ (0.1 mmol) and $Ni(acetylacetonate)_2$ (0.1 mmol) were also prepared under the same conditions.

Liquid cell preparation. We used home-made self-contained liquid cells, which were fabricated using a process similar to the process described in previous publications[27,39]. First, we deposited a thin layer of amorphous SiN_x (13 nm) on both sides of a silicon wafer (ultrathin silicon wafers: 100 μm, 4 in, p-doped, Virginia Semiconductor) using low-pressure chemical vapour deposition. Photolithography, wet KOH etching, thermal deposition of indium and liquid cell assembly were then carried out, step by step, to fabricate the liquid cells, and the gap between the two silicon nitride membranes of each liquid cell was defined by the thermally deposited indium layer (~100 nm). The liquid solution was loaded using a syringe with a Teflon tube: a droplet of ~100 nl liquid was loaded into one of the reservoirs and the liquid was drawn into the liquid cell by capillary force. Finally, the reservoirs were sealed with epoxy, which allowed the liquid to be kept inside the liquid cell for an extended period of time. Fabrication of the liquid cell was performed in the Marvell Nanofabrication Laboratory, University of California at Berkeley.

TEM imaging and image processing. A ThermoFisher (previously FEI F20 Tecnai) microscope equipped with a Gatan in situ direct detection camera (K2 IS) was used to record the high-resolution TEM (HR-TEM) Supplementary Videos 4–7. A temporal resolution of 2.5 ms and ~2k × 2k resolution were achieved. Images were acquired at a TEM magnification of ×180k, which resulted in a pixel size of 0.038 nm (0.38 Å per pixel), and a frame rate of 400 frames s^{-1} was used. For the K2 IS direct detection camera, the conversion factor was one incoming electron (at 200 kV) for 190 counts, that is 190 counts per e^-; the electron beam current density was thus calculated to be 2,000–8,000 e^- $Å^{-2}$ s^{-1}. The K2 IS direct detection camera detected electrons in each pixel by directly exposing a thin CMOS image sensor to the electron beam (this is different from traditional CCD cameras, which use a scintillator to convert electrons to photons). The elimination of the scintillator and the corresponding optical fibres leads to significant improvement in both sensitivity and resolution. The output image file was in binary format during recording, and was later extracted into DigitalMicrograph (DM) format. A JEOL 2100 microscope equipped with a CCD camera (Gatan Orius camera) and operated at 200 kV was used for taking low-magnification images and Supplementary Videos 1–3 and 8. These videos were recorded at a frame rate of 30 frames s^{-1}. An electron beam current density of 10–50 e^- $Å^{-2}$ s^{-1} was used. For ex situ experiments, an FEI Titan microscope (200 kV) equipped with EDS was used for elemental analysis and ex situ HR-TEM images. An FEI Super-X Quad windowless EDS detector based on silicon drift technology with a solid angle of 0.7 sr allowed elemental mapping with high signal-to-noise ratio. The images were acquired in HAADF STEM mode with a half convergence angle of 10 mrad.

It is noted that the initial time of the captured videos is arbitrary. To improve the signal-to-noise ratio of the high-resolution Supplementary Videos 4–7, we summed 10 frames in the sequential images in image post-processing (Supplementary Fig. 4). The sequential images in Figs. 2 and 3 were false-coloured using Adobe Photoshop software. All original images are available (Supplementary Figs. 5–8 and Supplementary Videos 4–7).

Liquid film thickness. The liquid thickness in a SiN_x liquid cell at the initial stage is expected to be 100 nm, which is defined by the liquid cell spacer thickness. However, thickness variations have been found during our thickness calibration using electron energy loss spectroscopy (EELS). During imaging, the thickness of the liquid film changes due to bubble generation and/or liquid flow upon electron beam illumination, so the initial thickness of the liquid layer does not have a significant impact on our experiments. The thickness variations are demonstrated by the image contrast changes in Supplementary Fig. 9, and the variations in a liquid cell estimated using EELS are shown in Supplementary Fig. 10. HR-TEM images were taken in areas with thinner liquid (~10–20 nm). Low-magnification images and videos were taken for various liquid thicknesses in the range of 10–60 nm. Despite the variations in liquid thickness, 2D growth involving 3D-to-2D transformations was observed, implying that such a 3D-to-2D transition is independent of liquid confinement.

Nucleation and growth of metal oxide nanoparticles and the electron beam effect. The nucleation and growth of metal oxide nanoparticles proceeds as a result of the electron beam decomposing the precursor solution[35]. The mechanisms of crystalline nanoparticle formation in a liquid cell have been reported in many other previous publications[27–29]. Calculations on electron beam induced minimum heating effects have also been reported previously[27]. It is worth mentioning that abundant solvents/ligands are presented during the nucleation and growth of the metal oxide nanoparticles under strong electron beam illumination in this work, as confirmed by the liquid flow shown in Supplementary Figs. 1a and 9. In each video, the electron beam current density was kept constant. Different electron current densities were used in our experiments. We found that the observed 2D growth characteristics are independent of the electron beam current density (Figs. 1–3 and Supplementary Fig. 1). The cobalt-based oxide can also transform from 3D nanoparticles to 2D nanosheets by shuttering the electron beam periodically and thus limiting electron beam exposure, as shown in Supplementary Fig. 11. Moreover, the electron beam does not cause damage to the growing inorganic nanocrystals in solution (Supplementary Figs. 5–8), where all the 2D nanosheets are crystalline with a rocksalt cubic structure. Both cobalt oxide and cobalt nickel oxide form 2D nanosheets, while nickel oxide prefers to maintain 3D nanoparticles throughout the growth, under the same conditions. These results suggest that the observed formation of 2D nanosheets involving 3D-to-2D transformations arises from the intrinsic material properties.

Growth trajectories of cobalt oxide nanosheets. The growth trajectory of a cobalt oxide nanosheet (shown in Supplementary Video 5) shows that the nanosheet resides along the [002] viewing axis, and the angle of 135° at the crystalline edges indicates the presence of highly reactive {220} facets. The sequential TEM images extracted from Supplementary Video 5 are shown in Supplementary Fig. 6, in which each of the (200), $(0\bar{2}0)$, $(\bar{2}\bar{2}0)$, and $(2\bar{2}0)$ facets is identifiable. We find that the $(\bar{2}\bar{2}0)$ and $(2\bar{2}0)$ facets continue to grow with faster rates than the (200) and $(0\bar{2}0)$ facets, which show anisotropic growth behaviour. The growth of all facets results in a flat nanosheet with a relatively stable structure.

Growth process of nickel oxide nanocrystals. The growth of nickel oxide nanocrystals was carried out under the same experimental conditions. The average size of the nanoparticles was 3.1 ± 0.4 nm at the early stage (12.8 s, Supplementary Fig. 15b) and 3.5 ± 0.9 nm in the later stage (355.2 s, Supplementary Fig. 15c). The crystal structure of the nanoparticles was confirmed by HR-TEM imaging and the composition by EDS elemental maps (Supplementary Fig. 17).

Ex situ TEM characterization. Before characterization, the as-obtained samples in the liquid cell were dried under an ambient environment for several hours and then opened. The samples were loaded into the TEM holder soon after opening to minimize exposure to air. The HR-TEM images show that both the nanoparticles and the nanosheets have a cobalt oxide rocksalt crystal structure (Supplementary Fig. 12).

Determining nanosheet thickness. To estimate the thickness of the cobalt oxide and cobalt nickel oxide nanosheets, we first tracked the nanocrystal growth trajectories of each system. We analysed the sizes of the nanoparticles as a function of time and found, within the measured time frame, that the size of the nanoparticles did not change. Supplementary Fig. 1b shows five representative nanoparticles (particles 1, 2, 5, 6 and 9), which were measured from the sequential TEM images in Supplementary Video 3 using Image J software. The size of each particle was kept constant until it transformed into a nanosheet (at ~30 s), during which the average size of the particles was 3.8 ± 0.3 nm (Supplementary Fig. 1c). There was no obvious attachment of atoms or clusters to the particle facets during the first part of the video. Once the transformation began, the measured 'core' particle sizes reduced as the material spread out to form a nanosheet at the edges (Supplementary Figs. 1b and 2a). We can assume that the mass of the nanoparticle was conserved during the 3D-to-2D transformation. Then, the thickness of the nanosheet was calculated to be ~1.0 nm (the total volume of all the particles is equal to the formed nanosheet). We also found similar growth behaviour in the binary cobalt nickel oxide nanoparticles (Supplementary Videos, and 2 and Supplementary Fig. 2a); most particles display no obvious growth before the transformation to the nanosheet. The particle transformation into a nanosheet occurred in Supplementary Video 1 at ~1.4 s (the initial time is arbitrary); the average size of these particles was 4.3 ± 0.7 nm based on statistical measurements of abundant nanoparticles under a large field of view (Supplementary Fig. 2b). At the early stage of growth (17.8 s; Supplementary Video 2), the thickness of the cobalt nickel nanosheet was ~1.1 nm. In the later stage of growth, the nanosheet fragments coalesced (Supplementary Video 1), and the thickness was reduced to 0.8 nm (at 154.2 s) and 0.6 nm (at 308.6 s), respectively. The nanosheet sizes were measured as 10–20 nm.

Oxygen elemental distribution. The oxygen map does not clearly define the crystal shape, unlike the cobalt and/or nickel elements shown in Fig. 1e,g; this is mainly due to a high concentration of oxygen presented in the dried organic solvents that becomes fixed to the cell during the drying process. Previous work has shown that the number of oxygen atoms in the residual solution per volume is only about one to two orders of magnitude less than that in a nanocrystal[39]. Thus, the shape of the nanocrystal in an oxygen map is not as sharp as in the metal element maps.

Ex situ synthesis of cobalt oxide nanosheets. To rule out the influence of the liquid confinement and electron beam effects, and to further confirm this 2D growth process has wider applicability, we carried out synthesis of cobalt oxide

nanosheets with a similar growth solution but outside the liquid cell TEM. In a typical procedure, the solution was prepared by dissolving 0.5 mmol of $Co(acetylacetonate)_2$ in a mixture of oleylamine, oleic acid and benzyl ether (4.5:4.5:1 in a volume ratio in a total 5 ml solution), and the mixture solution was transferred into a Teflon-lined autoclave (20 ml) and heated at 230 °C for 3 h. The final product was collected by centrifugation with alcohol several times. The as-obtained cobalt oxides show typical 2D morphologies (Supplementary Fig. 13).

We also synthesized cobalt oxides with *n*-butylamine and ethylene glycol (or ethyl alcohol) as the capping agents, respectively. The results show that cobalt oxide nanosheets can be achieved by using *n*-butylamine ligands (Supplementary Fig. 14a). However, when ethylene glycol was employed, the products show the typical 3D particle structures (Supplementary Fig. 14b). The above results demonstrate that the amine-based ligands play an important role in the formation of 2D metal oxides. However, when different surfactants are used, the growth mechanism may change; for example, large 3D particles can be obtained following the conventional nucleation and growth theories[40].

DFT calculations. The calculations were performed using the Vienna ab initio simulation package (VASP) with the projector-augmented wave method[41,42]. The generalized gradient approximation of Perdew–Burke–Ernzerhof (GGA-PBE) was adopted for the exchange-correlation functional[43]. The energy cutoff for the plane-wave expansion was set to 400 eV. Structure relaxation was stopped when the force on each atom was smaller than 0.02 eV $Å^{-1}$. The van der Waals interaction was included by using the correction scheme from Grimme[44].

To better understand the thermal dynamic driving force of the observed 3D-to-2D transformations, we estimated the total energy of the 3D nanoparticles and 2D nanosheets. Because a nanoparticle (~4 nm) with ligands can contain tens of thousands of atoms, practical DFT calculations are prohibitive. We used a simplified model by considering that each nanoparticle and nanosheet consists of surfaces, edges and bulk. The surface energy, edge energy and bulk energy of a small structure model can be calculated first. Then, the larger system is the sum of all these energies. For example, we first constructed a surface without an edge to obtain the surface energy, and then used a nanowire containing both surface and edge to obtain the edge energy. Such an approach is reliable because these energies are local properties (for example, they only depend on local structure, not on the global structure of the model) and the large system can be treated as the sum of local features.

Cobalt oxide calculations. To reproduce the anti-ferromagnetic ground state of cobalt oxide, we performed spin–polarization calculation by using the DFT + U approach with an effective U value of 3.5 eV. The optimized lattice constant of cobalt oxide is 4.24 Å, which agrees with the experimental value[45]. Bulk cobalt oxide is an anti-ferromagnetic semiconductor with a rocksalt structure; the spins of Co ions are altered along the [111] direction, but parallel within each (111) plane, namely the AFM-II configuration (Supplementary Fig. 17)[46]. The calculated magnetic moment on each Co atom is 2.7 bohr, and the bandgap is 2.32 eV. These values also agree with previous experimental data[47,48].

Areal density of amine on cobalt oxides. On the amine adsorbed cobalt oxide surface, the N atoms prefer to bind with the Co atoms due to their Coulomb interactions. The density of the amine is determined by considering that half of the Co atoms on the surface are bonded to amines (50% coverage). In this case, the amines are separated by a reasonable distance of 4–6 Å. Compared with lower coverage cases (say 25%), the surface energy of the 50% coverage case is lower due to more bonded amines. On the other hand, in the case of higher coverage (say 100%), the amine–amine distance can be quite small (less than 3 Å), and this could lead to a large repulsion between the amines and increases the surface energy. Therefore, in terms of a balance between the amine–surface binding and amine–amine repulsion, the 50% coverage case is the most possible structure. To further confirm this, we carried out further calculations using different amine coverage. It was found that with 25% coverage, the surface energy is 0.018 eV $Å^{-2}$. With 75% coverage, the surface energy is 0.024 eV $Å^{-2}$. With 50% coverage, the surface energy is −0.0017 eV $Å^{-2}$. Therefore, at 50% coverage, the surface can have minimum surface energy. This is a balance between the amine–surface binding and amine–amine repulsion as expected, thus the constructed model is reasonable.

The calculations of the amine adsorption energy were performed by choosing an isolated amine in a vacuum as the reference state. Normally, due to the highly coordinated environment in the actual experiment, the binding effect of amine in the solvent should be included. However, it is difficult to calculate the free energy of a solute in solvent and the implicit solvent model might not be adequate in this particular case. It is generally accepted that the alkyl chain interaction when the ligand is in the solvent and at the surface might cancel each other, but the amine end group can have interactions in the solvent. To estimate the binding effect of amine in the solvent, the amine–amine dimer was also chosen as the reference state to carry out the calculations of amine adsorption energy.

Here, we used the amine–amine dimer as the reference state to consider such a binding effect, following an approach similar to that in the literature[36]. In reality, there could be a van der Waals interaction between the side chains. However, such a side chain interaction between the molecules on the surface and the molecules in the solvent should be roughly the same, so they cancel each other (both can adjust themselves to the optimized chain–chain distance; for the molecules on the surface, this can be achieved by inclination). So, the only difference between the molecule on the surface and the molecule in the solvent is the dimer interaction. The binding energy of the dimer is about −0.1 eV per amine. Therefore, the amine–amine binding interaction is weak. Although in reality the configuration of oleylamine molecules under a solvent environment can be complex, the calculated adsorption energy should be insensitive to the reference state due to the weak amine–amine binding.

The optimized structures of the amine-adsorbed cobalt oxide (100) and (110) surfaces are shown in Supplementary Fig. 20, and the corresponding results for the adsorption calculations are listed in Supplementary Tables 1 and 2. It was found that both calculation models follow the same trend; that is, although a single amine binds more strongly to the (110) surface than to the (100) surface, the bare surface energy for (100) is much smaller than for (110), and the amine density for (100) is higher than for (110); with amine passivation the surface energy for (100) always become negative whereas that for (110) remains positive. It is noted that, due to the oleylamine ligands binding to the nanoparticle surfaces, a certain amount of oleylamine ligands can be adsorbed on the metal oxide surfaces during the 3D-to-2D transformations.

In addition to amines, other molecules, such as those with carboxyl (–COOH) and hydroxyl (–OH) groups, are also often used as capping agents for nanocrystal growth. Here, we carried out calculations for CH_3COOH and CH_3OH adsorbed on a CoO (001) surface. The results show that the surface energy became positive for both molecules (2 meV $Å^{-2}$ for CH_3COOH and 4 meV $Å^{-2}$ for CH_3OH). Therefore, growth with these two molecules does not lead to 2D morphologies, which is in agreement with the above experimental results.

To simulate the edges, we constructed a CoO nanowire terminated by the (100) and (010) surfaces and extending along the [001] direction, as shown in Supplementary Fig. 20. In our calculations, no edge reconstruction is observed. Although it is still possible that there could be another structure, the fact that we found a bandgap of 1.8 eV in the modelled structure indicates there is no obvious dangling bond state. The surface or edge reconstruction in such cases is less likely to occur. The calculated bare edge energy for the edge between neighbouring (100) surfaces is 143 meV $Å^{-1}$ without amine passivation. Amine binding can lower the edge energy by 69 meV $Å^{-1}$ with the inclusion of amine binding. Hence, the edge energy is determined to be 74 meV $Å^{-1}$.

Energy differences between a nanoparticle and a nanosheet for different nanosheet thickness. The total energy E_{3D} for a 3D cubic nanoparticle can be expressed as

$$E_{3D} = 6L_0^2E_s + 12L_0E_e + L_0^3E_b$$

and the total energy E_{2D} for a 2D nanosheet can be expressed as

$$E_{2D} = (2L^2 + 4LT)E_s + (4T + 8L)E_e + L^2TE_b$$

Here, L_0 is the edge length of the cubic nanoparticle, T is the thickness of the nanosheet and L is the lateral size.

The estimated energy difference between a 3D cubic particle and 2D sheet with the same volume V for different sheet thickness T is shown in Supplementary Fig. 21. When L_0 is small, the particle has lower energy, and when L_0 is large, the sheet has lower energy. The critical size increases as the thickness of the sheet increases.

Nickel oxide calculations. We used similar calculations on nickel oxide as used for cobalt oxide, with an effective U value of 4 eV. The structural and magnetic properties of nickel oxide are quite similar to those of cobalt oxide. The optimized lattice constant is 4.19 Å. It also has the AFM-II configuration. The calculated bandgap is 2.63 eV, and the magnetic moment on each Ni atom is 1.63 bohr. These results are consistent with a previous study[49].

We used the same model as used for cobalt oxide to estimate the total energy of the nickel oxide nanoparticle and nanosheet. The calculated bare (100) surface energy of nickel oxide is 52 meV $Å^{-2}$, so the calculated surface energy with passivation, edge energy and bulk energy are $E_s = -0.67$ meV $Å^{-2}$, $E_e = 163$ meV $Å^{-1}$ and $E_b = -559$ meV $Å^{-3}$, respectively. Supplementary Fig. 24a shows the estimated total energy difference between the nanoparticle and the 1.0-nm-thick nanosheet. When the size of the particle L_0 is larger than 18 nm, the nanosheet becomes more stable. Supplementary Fig. 24b shows the estimated kinetic barrier for the 3D-to-2D transition using the particle-sheet model as described in the main text (thickness of sheet $T = 1$ nm). When L_0 is larger than 47 nm, the barrier becomes zero. The critical size for the 3D-to-2D transition of nickel oxide is much larger than that of cobalt oxide. When the amine binding effect is considered, the amine binding reduces the energy by 46 meV $Å^{-2}$, the total (100) surface energy of nickel oxide is determined to be 6 meV $Å^{-2}$, and the positive surface indicates that the 3D-to-2D transition will not occur in nickel oxide particles. Thus, all the calculations show that it is much more difficult for such a transition to occur in the nickel oxide system.

Data availability

Data are available in the online version of this paper. Data that support the findings of this study are available from corresponding authors upon reasonable request.

Code availability

Computer codes for theoretical calculations in this work are available upon request from the corresponding authors.

References

39. Liang, W. I. et al. In situ study of spinel ferrite nanocrystal growth using liquid cell transmission electron microscopy. *Chem. Mater.* **27**, 8146–8152 (2015).
40. Xia, Y. N., Xiong, Y. J., Lim, B. & Skrabalak, S. E. Shape-controlled synthesis of metal nanocrystals: simple chemistry meets complex physics? *Angew. Chem. Int. Ed.* **48**, 60–103 (2009).
41. Blöchl, P. E. Projector augmented-wave method. *Phys. Rev. B* **50**, 17953–17979 (1994).
42. Kresse, G. & Furthmüller, J. Efficient iterative schemes for ab initio total-energy calculations using a plane-wave basis set. *Phys. Rev. B* **54**, 11169–11186 (1996).
43. Perdew, J. P., Burke, K. & Ernzerhof, M. Generalized gradient approximation made simple. *Phys. Rev. Lett.* **77**, 3865–3868 (1996).
44. Grimme, S. Semiempirical GGA-type density functional constructed with a long-range dispersion correction. *J. Comput. Chem.* **27**, 1787–1799 (2006).
45. Redman, M. J. & Steward, E. G. Cobaltous oxide with the zinc blende/wurtzite-type crystal structure. *Nature* **193**, 867 (1962).
46. Deng, H. X. et al. Origin of antiferromagnetism in CoO: a density functional theory study. *Appl. Phys. Lett.* **96**, 162508–162510 (2010).
47. Imada, S. & Jo, T. Magnetic states of cobalt oxide and ferrites and magnetic dichroism in 2*p*-3*d* X-ray absorption spectroscopy. *J. Magn. Magn. Mater.* **104**, 2001–2002 (1992).
48. van Elp, J. et al. Electronic structure of CoO, Li-doped CoO and $LiCoO_2$. *Phys. Rev. B* **44**, 6090–6103 (1991).
49. Schrön, A., Granovskij, M. & Bechstedt, F. Influence of on-site Coulomb interaction U on properties of MnO(001) 2×1 and NiO(001) 2×1 surfaces. *J. Phys. Condens. Matter* **25**, 094006–094015 (2013).